Biosensors and Bioelectronics 25 (2009) 275–281

Contents lists available at ScienceDirect

Biosensors and Bioelectronics

journal homepage: www.elsevier.com/locate/bios

Spectral-domain optical coherence phase microscopy for label-free multiplexed protein microarray assay

Chulmin Joo[a,b,*], Emre Özkumur[c], M. Selim Ünlü[c], Johannes F. de Boer[a,d,**]

[a] Wellman Center for Photomedicine, Harvard Medical School and Massachusetts General Hospital, Boston, MA 02114, United States
[b] Dept. of Mechanical Engineering, Massachusetts Institute of Technology, Cambridge, MA 02139, United States
[c] Dept. of Electrical and Computer Engineering, Boston University, Boston, MA 02139, United States
[d] Dept. of Physics and Astronomy, VU University, 1081 HV Amsterdam, The Netherlands

ARTICLE INFO

Article history:
Received 23 April 2009
Received in revised form 12 June 2009
Accepted 16 June 2009
Available online 24 June 2009

Keywords:
Optical interferometer
Optical coherence tomography
Label-free
Microarray
Proteomics

ABSTRACT

Quantitative measurement of affinities and kinetics of various biomolecular interactions such as protein–protein, protein–DNA and receptor–ligand is central to our understanding of basic molecular and cellular functions and is useful for therapeutic evaluation. Here, we describe a laser-scanning quantitative imaging method, referred to as spectral-domain optical coherence phase microscopy, as an optical platform for label-free detection of biomolecular interactions. The instrument is based on a confocal interferometric microscope that enables depth-resolved quantitative phase measurements on sensor surface with high spatial resolution and phase stability. We demonstrate picogram per square millimeter surface mass sensitivity, and show its sensing capability by presenting static and dynamic detection of multiplexed protein microarray as immobilized antigens capture their corresponding antibodies.

1. Introduction

Sensitive and selective methods to detect molecular affinity and kinetics are important tools in molecular and cell biology, medicine, and environmental monitoring. For instance, knowledge of multitudes of biomolecular interactions is essential to understanding signal transduction pathways of cells (Cooper and Hausman, 2006). Medicine has an obvious need for highly sensitive detection methods for various molecular disease signatures and viruses, and early detection of chemicals and pathogens (e.g., anthrax) that could trigger corrective action is also of significance in environmental applications.

The vast majority of sensing schemes typically employ secondary agents conjugated to captured molecules, which are subsequently detected with either fluorescent or enzyme-linked reagents. These methods have been widely utilized and successful for the detection of nucleic acid interactions in microarrays (Heller, 2002), since the structure and reactivity of nucleic acids are relatively uniform and minimally influenced by the secondary agents. However, the structure and reactivity of proteins are much more complex and diverse than those of DNA, and the attachment of the secondary agents to proteins is likely to alter kinetic characteristics of the proteins to other molecules (MacBeath, 2002). The efficiency of labeling may also vary from protein to protein, making it difficult to realize high-throughput protein assay (Mitchell, 2002). Noting these issues, there is a rising need for label-free techniques that enable direct monitoring of biomolecular interactions without secondary agents.

Various types of label-free optical biosensors have been investigated, which include sensors based on surface plasmon resonance (SPR) (Homola, 2006), reflectometric interference spectroscopy (Birkert et al., 2002), ring micro-resonators (Armani et al., 2007; Vollmer and Arnold, 2008), and interferometry (Bornhop et al., 2007; Yalcin et al., 2006). Among these detection methods, interferometric measurements can potentially provide high sensitivity to phase change, achieving better than 10^{-10} rad resolution (Ando et al., 2001). Mach–Zehnder interferometers have been integrated with SPR for differential phase measurements (Wu et al., 2004), and Young interferometers were implemented with optical waveguides of which surfaces were activated with probe molecules (Ymeti et al., 2007). Common-path in-line shearing interferometer demonstrated ~pg/mm^2 level surface mass sensitivity (Zhao et al., 2008). Recently, spectral reflectance imaging biosensor (SRIB) has

Abbreviations: OCT, optical coherence tomography; SD-OCT, spectral-domain optical coherence tomography; SD-OCPM, spectral-domain optical coherence phase microscopy; HSA, human serum albumin; αHSA, anti-HSA; BSA, bovine serum albumin; IgG, immunoglobulin G; PBS, phosphate buffered saline; PBST, PBS with Tween 20; αRO, anti-rabbit IgG; αMO, anti-mouse IgG.

* Corresponding author. Present address: GE Global Research, 1 Research Circle, Niskayuna, NY 12309, United States. Tel.: +1 518 387 4310; fax: +1 518 387 7021.
** Corresponding author. Present address: Dept. of Physics and Astronomy, VU University, 1081 HV Amsterdam, The Netherlands. Tel.: +1 31 20 598 7972.
E-mail addresses: jooc@ge.com (C. Joo), jfdeboer@few.vu.nl (J.F. de Boer).

0956-5663/$ – see front matter © 2009 Elsevier B.V. All rights reserved.
doi:10.1016/j.bios.2009.06.028

demonstrated high-throughput label-free protein assay based on the change of interference signature from reflected light upon the protein absorption (Özkumur et al., 2008).

Spectral-domain optical coherence phase microscopy (SD-OCPM) (Joo et al., 2005, 2007) is a quantitative phase imaging modality capable of generating depth-resolved amplitude and quantitative phase images of transparent specimens. Based on a common-path low-coherence interferometer, it has a picometer-level optical path-length sensitivity, and has been employed for quantitative visualization of structures and dynamics of cellular specimens without any exogenous contrast agents. Unlike other quantitative phase imaging techniques based on the transmitted light through a specimen (Choi et al., 2007; Popescu et al., 2004), SD-OCPM operates in reflection and allows simultaneous phase measurements on multiple interference signals of interest along the optical axis.

Here, we describe the first, to our knowledge, demonstration of the utility of a quantitative phase microscope, or SD-OCPM as a label-free screening tool for multiplexed protein microarray. Interference spectrum produced by the superposition of the reflected light from the sensor chips is measured and converted into complex-valued depth profile. We measure the shift of the interference signal of interest to quantify the molecular absorption and desorption on the sensor surface. We demonstrate picogram per square millimeter protein mass sensitivity, and present its detection capability through dynamic binding measurements of multiple analytes on immobilized probes. The advantages and the aspects for the improvement will also be discussed.

2. Materials and methods

2.1. SD-OCPM principle of operation

The basic principle of SD-OCPM is identical to that of spectral-domain optical coherence tomography (SD-OCT), as detailed elsewhere (Fercher et al., 1995; Nassif et al., 2003). Briefly, SD-OCT is based on a low-coherence spectral interferometer in which interference of reference and measurement light is spectrally dispersed, detected, and converted into path-length resolved amplitude and phase distribution of a specimen.

For optical path-length differences between reference and measurement optical waves, the spectrum related to interference can be written as:

$$I(k) = 2\sum_{n}[R_r R_s(z_n)]^{1/2} S(k)\ \cos(2kz_n), \tag{1}$$

where k is the wave number, z_n is the path-length difference between reference surface and the nth surface in the sample, and R_r and $R_s(z_n)$ represent reflectivity of the reference surface and the nth measurement surface, respectively. $S(k)$ is the spectral density of light source. A path-length resolved depth profile, $F(z)$, is obtained by an inverse Fourier transform of Eq. (1) with respect to $2k$, giving:

$$F(z) = \sum_{n}[R_r R_s(z_n)]^{1/2}\, \Gamma(z - z_n). \tag{2}$$

Here, $\Gamma(z)$ is referred to as the complex coherence function, directly related to the inverse Fourier transform of the source spectrum, $S(k)$. For a Gaussian light source centered at k_0 with a full width at half maximum (FWHM) bandwidth Δk, the complex coherence function is given by

$$\Gamma(z) \propto e^{i2k_0 z} e^{-4\ \ln 2(z/l_c)^2}, \tag{3}$$

and the coherence length, l_c, defined by the FWHM of $\Gamma(z)$ is evaluated as (Fercher et al., 2003):

$$l_c = \frac{2\ln 2}{\pi}\frac{\lambda_0^2}{\Delta\lambda}. \tag{4}$$

Here, λ_0 and $\Delta\lambda$ denote the center wavelength and the FWHM bandwidth in wavelength, respectively. The amplitude and phase of $F(z)$ are examined to construct structural and functional SD-OCT images, where the amplitude represents the specimen reflectivity and the phase change, which can be expressed as:

$$\Delta\phi = 2k_0\,\Delta z = \frac{4\pi}{\lambda_0}\,\Delta z, \tag{5}$$

corresponds to the change in refractive index and physical distance of a reflector in the sample relative to the reference.

Unlike typical SD-OCT imaging, SD-OCPM employs the light reflected from a surface along the probe beam path as a phase reference. Such a common path interferometer provides superior rejection of common mode phase noise, such as vibrations and temperature drifts, compared to the conventional interferometers where reference and measurement arms are separate. Fig. 1 depicts the SD-OCPM configuration for protein microarray screening in which the light reflected from the interface of Si–SiO_2 serves as a reference. The measurement light is back reflected from the optical focus on the medium–SiO_2 interface.

For a given oxide layer thickness, the interference of the reference (Si–SiO_2 interface) and measurement (medium–SiO_2 interface) light leads to an interference spectrum as a function of wavelength (Fig. 1(c)). Fig. 1(d) shows the distribution of the real component of the depth profile that is obtained by taking an inverse Fourier transform of the measured interference spectrum. Upon the absorption of proteins, the longer path-length causes the shift of the coherence function (shown in green). This shift can be quantified by examining a phase delay of the coherence function, indicating the protein absorption on the sensor surface. We interpret this phase alteration as a change in thickness at a constant refractive index of 1.45, commonly used as the refractive index of a monolayer of protein (Piehler et al., 1996). Using this approximation, optical thickness to molecular mass conversion follows as: ~1 pm thickness change is interpreted as ~1 pg/mm^2 of binding material on the surface.

In a fiber-based implementation of the presented SD-OCPM, the core in the single-mode fiber acts as a pinhole similar to confocal microscopy. Therefore, the lateral resolution is determined by focusing and collection optics as in confocal microscopes (Wilson, 1990). The axial resolution of SD-OCPM, on the other hand, is determined by the combination of confocal and coherence gatings. In addition to the confocality provided by the use of a fiber core as a pinhole, the use of low-coherence interferometer confines the focal volume further by the coherence length of the light source.

2.2. SD-OCPM experimental setup

An 800 nm Kerr-lens mode-locked Ti:sapphire laser with a FWHM bandwidth of ~130 nm (Femtolasers, Austria) illuminated a single-mode fiber-based 2 × 2 coupler (Corning flexcore 780 fiber, AC Photonics, Inc.), of which the reference arm was not used.

The beam emitted from the sample arm fiber was collimated by the collimator with a $1/e^2$ diameter of ~3.4 mm, and passed through the galvanometer-driven scanners (Cambridge Technology, Inc., MA) employed for lateral beam scanning. Alternatively, sample could be scanned under the probe beam. A beam expander magnified the beam diameter to overfill the back-aperture of the objective, thereby fully utilizing the numerical aperture (NA) of the microscope objective.

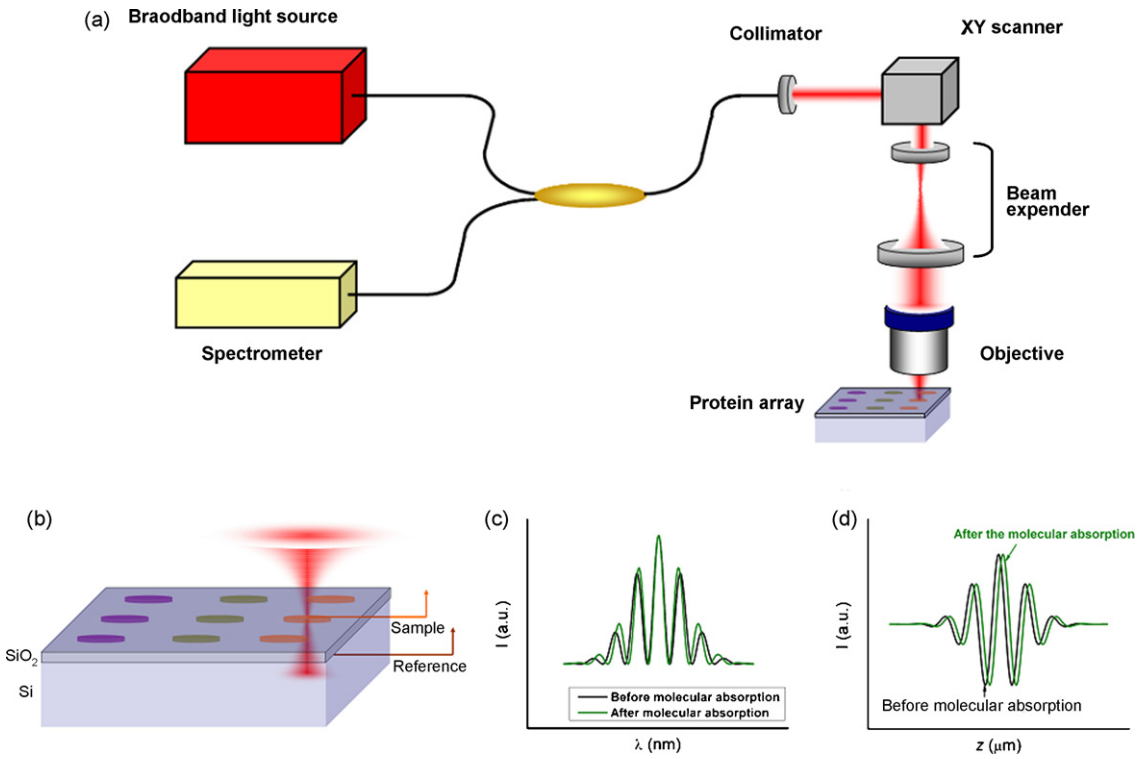

Fig. 1. (a) SD-OCPM for label-free protein microarray screening. A broadband light source is coupled to a fiber-based common-path interferometer. The light from the sample arm passes through galvanometer-driven scanners, magnified by a beam expander, and subsequently focused onto a sensor surface. The back-reflected light from the focal volume and from the interfaces along the beam path is re-coupled to the fiber-based interferometer, and the interference spectrum is measured at the spectrometer in the detection arm. (b) Phase distribution across the sensor surface is measured relative to the reference light reflected from the Si–SiO_2 interface. (c) Upon the absorption of protein layer, the induced longer path-length leads to the change in the frequency of the interference fringes. (d) This change translates into the shift of coherence function in the depth profile, which can be quantified by the phase measurement of the coherence function.

A microscope objective (LD Plan-NEOFLUAR, 5×/0.13, Zeiss, Germany) delivered light onto the specimen with a measured lateral FWHM resolution of ~2.5 μm. The light back reflected from the interfaces along the probe beam path was re-coupled into the fiber interferometer, and subsequently detected by a spectrometer. We built a high-speed spectrometer to acquire the cross-spectral density of reference and measurement light in the shot-noise limited regime (Joo et al., 2005; Nassif et al., 2003). The beam emitted by the detection arm fiber was collimated by a lens with a focal length of 100 mm, and incident on a volume holographic phase grating (1200 lines/mm, Wasatch Photonics, Inc.) at the Bragg angle. The spectrally dispersed light was then focused by a three-element air-spaced lens onto CCD arrays of 2048 elements (Line scan camera, L-104k, Basler, Germany, 10 μm × 10 μm pixel size). The maximum readout rate of the camera was 29 kHz and the acquired spectra could be transferred continuously to the host computer by CameraLink at a resolution of 10 bits/pixel. A frame grabber (PCI-1428, National Instruments) installed in the host computer managed the acquisition of spectra.

2.3. Data analysis

The measured interference spectra were first transformed from λ- to *k*-space using the method described by Mujat et al. (2007). Inverse Fourier transform of the transformed spectrum of interference results in path-length resolved complex profile at a position (*x*, *y*) on a specimen. We located the interference signal of interest with a known optical thickness of oxide layer, and examined its phase in space and time. Each SD-OCPM image is constructed as the probe beam scans across the chip.

For dynamic binding measurements, an initial reference image was subtracted from all subsequent images. The resulting phase difference images show any increase/decrease observed upon the specific association/dissociation of a target–probe complex. The resulting thickness was converted to mass density, and reported in the dynamic sensorgrams.

Calculation of association and dissociation rates was performed based on pseudo first-order kinetic model (Homola, 2006). The association and dissociation processes are symbolized by

$$A + B \xrightarrow{k_a} AB, \tag{6}$$

$$A + B \xleftarrow{k_d} AB, \tag{7}$$

where A is the concentration of in-solution free analytes, B is the amount of immobilized probe molecules, and AB is the complex. k_a and k_d represent on and off rate, respectively. In a typical sensor platform employing flow cells, the concentration of the free analytes is primarily maintained by flowing solution, and its corresponding processes can be modeled with the first-order kinetic model as:

$$AB(t) = \frac{k_a A_0 B_0}{k_a A_0 + k_d}[1 - e^{-(k_a A_0 + k_d)t}] \tag{8}$$

where A_0 and B_0 represent the concentration of each species at $t = 0$. We used least-squares method to fit the first-order exponential functions to the recorded sensorgrams, and solved for k_a and k_d.

2.4. Surface preparation

For the SD-OCPM proteomic assay, the sample can be a static proteomic microarray chip or microfluidic device with functionalized sensor surfaces. As a basic substrate, we used a silicon wafer with a top layer of thermally grown silicon dioxide (SiO_2) as the solid support for probe molecules. Silicon samples were

chemically and mechanically polished to better than 0.4 nm roughness as measured by atomic force microscopy (AFM), followed by thermal growth of an oxide layer. Thermal oxide growth process is self-limiting and provides highly uniform surfaces, virtually eliminating noise associated with variations in oxide thickness.

The cleaning and modification of SiO_2 surface for the covalent attachment of probe proteins has been performed, following the protocol described by Schena (2005). The surfaces were first cut into approximately 15 mm × 15 mm squares and cleaned by sonication in acetone, rinsed in methanol followed by a rinse with deionized water (dIH_2O). The chips were then placed in a solution of 10% NaOH for 10 min, rinsed in dIH_2O and dried under argon. The dried chips were epoxysilanized by immediately placing them in a solution of 3% (V/V) 3-(glycidoxypropyl)trimethoxysilane (United Chemical Technologies, Inc.) in toluene for 3 min and then rinsed for 5 min in toluene. Samples were then dried under argon, covered and placed in a vacuum desiccator and stored up to 2 months before use. All reagents were of high performance liquid chromatography (HPLC) quality and purchased through Sigma–Aldrich.

2.5. Protein spotting

The epoxysilanized chips were spotted with a desktop spotting unit (Odyssey Calligrapher minarrayer, Bio-Rad). For the initial static experiment, bovine serum albumin (BSA) (Sigma, A9085) and biotin–BSA (bBSA) (Sigma, A8549) were spotted at 1 mg/ml concentration in PBS (Fisher, pH 7.4) containing 2% glycerol (to prevent the spot evaporation).

For the dynamic binding experiment, BSA, human serum albumin (HSA) (Sigma, A9511), rabbit-immunoglobulin G (IgG) (Sigma, I5006), and mouse-IgG (Sigma, I5381) were spotted on epoxysilanized slides, all with 1 mg/ml concentration in PBS and 2% glycerol. The wafers were allowed to incubate for at least 1 h in the Bio-Rad Calligrapher humidity chamber (55% humidity) at room temperature before being stored overnight (O/N) in the presence of dessicant at 4 °C.

2.6. Assay procedure

For the dynamic interaction experiments, the chip was enclosed in a custom-made flow chamber. The chamber has a volume of ~1 ml and has an anti-reflection coated front glass window. Solutions were driven by a peristaltic pump at a rate of 400 μl/min. BSA (1 mg/ml) in PBS and Tween 20 (PBST) was initially flowed through the fluidic system to block the associated tubing and the flow cell, thereby minimizing the non-specific bindings to those surfaces. A flow of PBST was then followed for ~15 min to remove any weakly bound probes before any tests were performed. Dynamic interactions on BSA, HSA, rabbit IgG, and mouse IgG spots were observed upon the addition of polyclonal antibodies of rabbit-originated anti-HSA (αHSA) (Sigma, A0433), goat-originated anti-rabbit IgG (αRO) (Sigma, R1131), and goat-originated anti-mouse IgG (αMO) (Sigma, M5899), respectively, each analyte with the same concentration of 10 μg/ml.

3. Results

3.1. SD-OCPM performance

We first quantified performance of SD-OCPM by imaging a SiO_2 etch pattern array designed and fabricated to model a protein array chip. In a typical biochip assay, the analytes bind to the ligands on sensor surface, and the average signal change over the multiple activated sites is measured to detect binding events.

To mimic this scenario, we fabricated a ~10 μm thick SiO_2 substrate into which a 5 × 5 square pattern was etched using standard photolithography and wet etching techniques. In practice, it is difficult to achieve a precise control on the etch depth in each square pattern. Therefore, we distributed smaller square patterns (1 μm × 1 μm) in the larger 100 μm × 100 μm square as depressions, so that the number of open/closed smaller square patterns determined the average depth at each of 25 squares. That is, more of the depressions, the less the average thickness of the oxide layer.

Fig. 2 shows the SD-OCPM phase image of the model specimen. For imaging, the beam was focused and scanned on the oxide layer. The image size was 512 × 512 pixels, and the total acquisition time was ~27 s with a pixel integration time of ~4 μs. Each larger square has dimensions of 100 μm × 100 μm. Note that SD-OCPM visualized the density of depressions clearly. The average phase delay across the 30 × 30 pixels inside square patterns was calculated and plotted based on the density of depressions pre-determined from the mask design (Fig. 2(b)). The 0% in the density of depression represents no etching in the region. The change of average depth was not linear by the change in density of depressions, which is caused by the complications of using standard photolithography to make very small (1 μm × 1 μm) square patterns. The SD-OCPM measured depths were confirmed with an atomic force microscope and a commercial white light interferometer (Zygo). The noise-equivalent phase was estimated by taking the standard deviation in the region with no features (30 × 30 pixels), and found to be ~3.7×10^{-4} rad, which is translated into ~24 pm in optical thickness using Eq. (5).

3.2. Label-free detection of static biotin–streptavidin array

As an exemplary demonstration of static protein microassay chip imaging, an array of BSA and biotinylated BSA patterns after

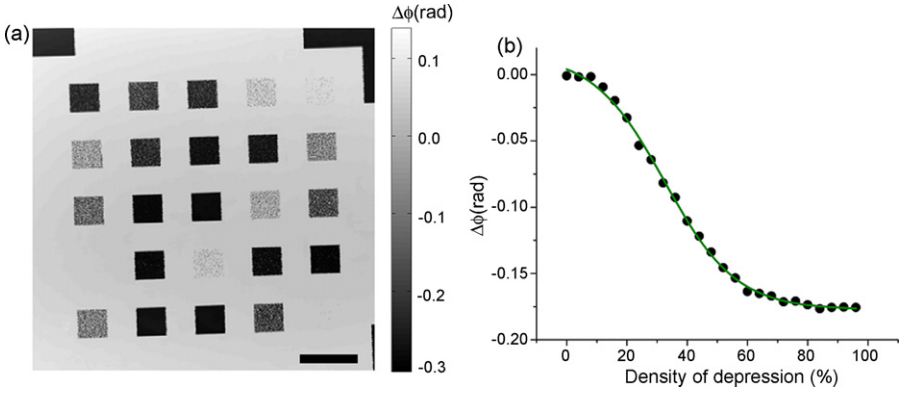

Fig. 2. (a) SD-OCPM phase image of 5 × 5 SiO_2 square etch patterns. Each square has a size of 100 μm × 100 μm. The maximum etch depth was ~7 nm. The scale bar denotes 200 μm. (b) Etch depth vs. depression level (0% depression level corresponds to no etching in the region).

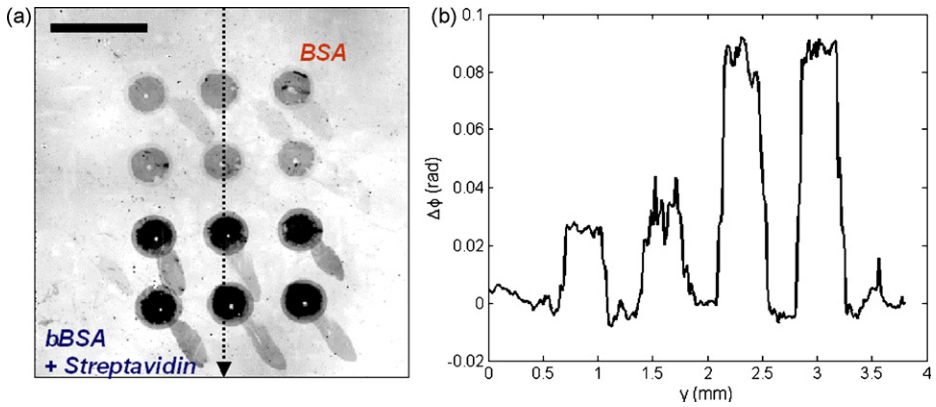

Fig. 3. SD-OCPM protein assay on selective absorption of streptavidin to bBSA. The BSA and bBSA were spotted on the sensor surface. After incubation with streptavidin solution and rinsing with PBST, a ~0.055 rad increase in phase delay was observed on bBSA spots, relative to BSA spots. (a) SD-OCPM image on sensor chip. The scale bar represents 1 mm. (b) Phase distribution along the line indicated in (a).

streptavidin incubation was imaged. The SiO_2 surface was functionalized with epoxy group for covalent attachment of proteins. After spotting BSA and bBSA and O/N incubation, the substrate was washed 3× with PBS containing 0.1% Tween 20 (Sigma–Aldrich Co., MO), 3× with PBS, and 1× with deionized water. Then the sample was incubated with streptavidin at a concentration of 5 μg/ml for 1 h, and washed with the same washing procedure. The sample was then dried under an inert gas before measurement.

Fig. 3 shows SD-OCPM image of the array and the phase distribution along the line denoted in the image. It can be seen that specific binding affinity of streptavidin to biotin–BSA is observed by an increase in optical thickness. The average phase delay due to the binding of streptavidin onto biotin–BSA patterns relative to the BSA patterns was measured as ~0.055 rad, which corresponds to ~2.4 nm in physical thickness, with an assumed protein refractive index of 1.45.

3.3. Dynamic detection of multiplexed biomolecular interactions

To measure the binding dynamics, the sensor chip was placed in a custom-made flow chamber sealed with a transparent glass window. Four different probes were spotted on an epoxysilanized chip and their interactions with various analytes were monitored as a function of time (Fig. 4). At the beginning of data acquisition, the flow elements and the sample surface were first blocked by 0.1 mg/ml BSA in PBST, and then washed with PBST.

Fig. 4 shows the time evolution of the accumulated mass density averaged over 5 spots for each probe. SD-OCPM images of the change in phase distribution were acquired at 30 s/frame with an image size of 256 × 256 pixels. The phase delay in each spot was measured relative to the nearby non-activated SiO_2 surface to eliminate non-specific noise factors, and converted to the accumulated mass density as described in Section 2.1. The inset images show 20 spots in 4 rows at different stages of the experiment. Following the first PBST flow for 5 min, rabbit-originated anti-HSA (αHSA) in PBST (10 μg/ml) was reacted for ~40 min and ~1.4 nm and ~2.3 nm thickness increases were detected at both BSA and HSA spots, respectively. The polyclonal rabbit-originated αHSA bound to both BSA and HSA spots, as a ~76% sequence identity exists between BSA and HSA. Measurable dissociation was observed when the chip was washed with PBST alone ($t \sim 70$ min). Subsequently, goat-originated anti-rabbit IgG (10 μg/ml) was introduced, and thickness increases in all the spots were detected. Not surprisingly, we measured the bindings of anti-rabbit IgG (αRO) on the rabbit IgG spots. The associations of anti-rabbit IgG on the BSA and HSA spots can be accounted for by the previous binding of the αHSA to the BSA and HSA spots. The αHSA is rabbit-originated, so the anti-rabbit IgG binds to the αHSA, which is on top of the BSA and HSA spots. The number of the rabbit-originated αHSA molecules immobilized on HSA and BSA spots is likely to be greater than the number of rabbit IgG molecules on the surface after multiple washing procedures. Therefore, more of αRO bindings are seen on the HSA and BSA spots because of the increased number of available binding sites. Note that cross-reactivity was also detected between anti-rabbit IgG and the spotted mouse IgG as well. Some dissociation was seen again during PBST wash at ~95 min. Next, rabbit anti-mouse IgG (10 μg/ml) was flowed, and the thickness increase more pronounced at mouse IgG spots.

Kinetic association and dissociation coefficients can readily be obtained from the sensorgram measured from each spot. As an exemplary case, Fig. 5(a) shows the sensorgram for each BSA and HSA spot during αHSA injection. We extracted the association and dissociation coefficients averaged over 5 spots in each case, and found to be $k_a = (1.37 \pm 0.08) \times 10^4\ M^{-1}\ s^{-1}$ and $k_d = (7.80 \pm 0.99) \times 10^{-5}\ s^{-1}$ for BSA and $k_a = (2.61 \pm 0.05) \times 10^4\ M^{-1}\ s^{-1}$ and $k_d = (3.92 \pm 0.50) \times 10^{-5}\ s^{-1}$ for HSA (Fig. 5(b) and (c)). The corresponding k_d for BSA and HSA spots were 5.7 nM and 1.5 nM, respectively. The measured association rates for αHSA–BSA and αHSA–HSA were consistent with the reported results using

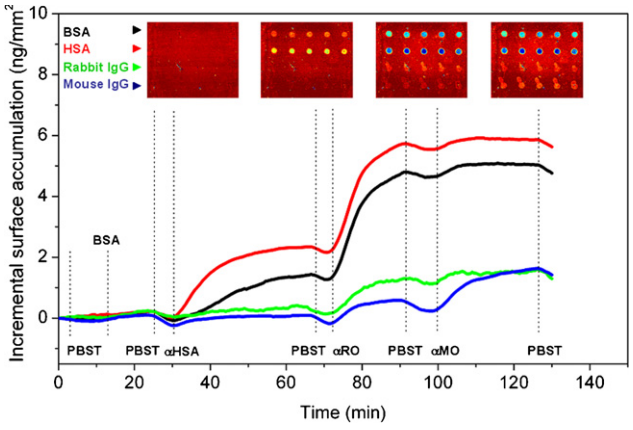

Fig. 4. Dynamic kinetic measurements of antibodies binding to different antigens. The sensorgrams were generated by averaging phase change over 5 spots for each probe molecule. The noise-equivalent thickness fluctuation in time was ~7 pm per spot. Insets show the SD-OCPM images at different stages of the experiment. PBST: PBS buffer with Tween 20, αHSA: rabbit-originated anti-HSA, αRO: goat-originated anti-rabbit IgG, and αMO: goat-originated anti-mouse IgG.

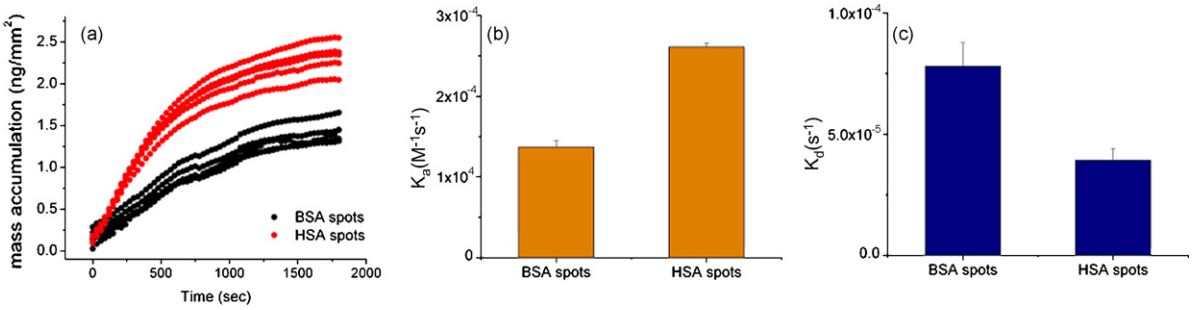

Fig. 5. Calculated kinetic association and dissociation parameters for BSA and HSA spots with αHSA. (a) Sensorgrams for each spot and (b and c) present k_a and k_d averaged over 5 spots for each species. The error bar denotes standard deviation.

SRIB to within ~20% (Özkumur et al., 2008). A compressed-time movie of this experiment is provided as Supplemental Material (SI Video 1). The baseline noise was ~7 pm per spot during in-solution measurements, and averaging over 5 spots for the same probe reduced the noise floor to less than ~5 pm, corresponding to a limit of detection better than ~5 pg/mm^2 bound target.

4. Discussion

Based on a short coherence length and high phase stability provided by a common-path low-coherence interferometer, SD-OCPM measures the phase delay of the surface of interest without the effect of other surfaces and solution temperature/concentration fluctuations. This feature is highly attractive in sensor applications, since refractive index change in bulk solutions due to a temperature drift is a significant noise factor in other surface-sensitive sensor methods based on SPR and evanescent waves. The lateral resolution of SD-OCPM is determined by focusing and collection optics, providing higher spatial resolution compared to other full-field imaging methods. Though it may not be critical to sensor applications where one takes an average over many activated sites to improve sensitivity, the ability for high-resolution imaging can be advantageous when the number of probe molecules is limited or when multiple probe species need to be positioned closely for sensor miniaturization.

SD-OCPM exhibits distinct advantages and drawbacks compared to other high-throughput optical biosensors. Ellipsometric and SPR imaging techniques have demonstrated screening of protein arrays (Gao et al., 2006; Wegner et al., 2004; Shumaker-Parry and Campbell, 2004). These techniques, though, require oblique incidence of light beams and polarization control as opposed to normal upright microscope configuration in SD-OCPM, which may be attractive for high-resolution, high-density protein microarray screening. The common-path quadrature interferometric method provides a cheap and highly sensitive screening for multiplexed protein microarray (Zhao et al., 2008). However, the use of quadrature interferometer based on the oxide layer thickness requires precise thickness control of better than 10 nm for a given wavelength, as it determines dynamic range for molecular absorption. SD-OCPM, in contrast, can resolve the interference signal as long as the oxide layer thickness is more than the coherence length of the light source. In terms of the spectroscopic measurement and phase delay analysis, our technique is similar to the recent advances in reflectometric interference spectroscopy (Birkert et al., 2002; Gauglitz, 2005) and SRIB (Özkumur et al., 2008). These methods employ a 2D CCD detector, and scan the wavelengths either with a white-light source and wavelength filter wheels or wavelength-tunable laser. SD-OCPM, on the other hand, measures the spectrum at a lateral position and scans the beam across the sensor surface.

The presented SD-OCPM was implemented for high-resolution imaging of cells and tissues, which requires a high-power ultra-broadband light source and high spectral resolution 2048-element spectrometer. As for the screening of protein microarrays, though, one can employ less expensive low-power broadband light source and spectrometer. For instance, commercially available broadband superluminescent laser diodes or light emitting diodes are much cheaper and provide a spectral bandwidth of more than 30 nm, which corresponds to a coherence length of <6 μm. Therefore, so long as the oxide layer thickness is more than the coherence length, SD-OCPM can resolve the shift of the corresponding coherence function, and measure phase alternation due to molecular absorption. A commercially available miniature spectrometer with a smaller number of elements can also be used with a higher readout rate.

5. Conclusion

We presented SD-OCPM as an optical method for label-free, multiplexed assay of protein microarray. We demonstrated picometer-level thickness sensitivity of SD-OCPM, and employed the method to measure specific binding of streptavidin to bBSA spots. SD-OCPM was further utilized to detect dynamic molecular interactions of multi-analytes in a fluidic format with better than ~7 pg/mm^2 mass sensitivity per spot, and ~5 pg/mm^2 by averaging over 5 spots.

As a functional derivative of SD-OCT, SD-OCPM has been used for label-free imaging of cellular structure and dynamics with high path-length sensitivity. The presented work demonstrates an extension of SD-OCPM application to molecular biology as a protein microarray-screening tool.

Acknowledgements

This work was supported by grants from National Institute of Health (R01 RR19768, EY14975 to J.F.dB), the U.S. Department of Defense (F4 9620-01-1-0014 to M.S.U.), Army Research Laboratory (W911NF-06-2-0040 to M.S.U.), and the Center for Integration of Medicine and Innovative Technology. The authors are grateful to Drs. Ki Hean Kim and Conor Evans for their contributions to the system setup. C.J. would like to thank the support through Wellman Graduate Fellowship and Hatsopoulous Innovation Award from the MIT Department of Mechanical Engineering.

Appendix A. Supplementary data

Supplementary data associated with this article can be found, in the online version, at doi:10.1016/j.bios.2009.06.028.

References

Ando, M., Arai, K., Takahashi, R., Heinzel, G., Kawamura, S., Tatsumi, D., 2001. Physics Review Letters 86 (18), 3950–3954.

Armani, A.M., Kulkarni, R.P., Fraser, S.E., Flagan, R.C., Vahala, K.J., 2007. Science 317 (5839), 783–787.
Birkert, O., Tünnemann, R., Jung, G., Gauglitz, G., 2002. Analytical Chemistry 74 (4), 834–840.
Bornhop, D.J., Latham, J.C., Kussrow, A., Markov, D.A., Jones, R.D., Sørensen, H.S., 2007. Science 21 (5845), 1732–1736.
Choi, W., Fang-Yen, C., Badizadegan, K., Oh, S., Lue, N., Dasari, R.R., Feld, M.S., 2007. Nature Methods 4, 717–719.
Cooper, G.M., Hausman, R.E., 2006. The Cell: A Molecular Approach, 4 ed. Sinauer Associates, Inc.
Fercher, A.F., Drexler, W., Hitzenberger, C.K., Lasser, T., 2003. Reports on Progress in Physics 66, 239–303.
Fercher, A.F., Hitzenberger, C.K., Kamp, G., El-Zaiat, S.Y., 1995. Optics Communications 117, 43–48.
Gao, T., Lu, J., Rothberg, L.J., 2006. Analytical Chemistry 78 (18), 6622–6627.
Gauglitz, G., 2005. Review of Scientific Instruments 76, 062224.
Heller, M.J., 2002. Annual Review of Biomedical Engineering 4, 129–153.
Homola, J., 2006. Surface Plasmon Resonance Based Sensors. Springer, Berlin.
Joo, C., Akkin, T., Cense, B., Park, B.H., Boer, J.F.d., 2005. Optics Letters 30 (16), 2131–2133.
Joo, C., Kim, K.H., Boer, J.F.d., 2007. Optics Letters 32 (6), 623–625.
MacBeath, G., 2002. Nature Genetics 32, 526–532.
Mitchell, P., 2002. Nature Biotechnology 20, 225–229.
Mujat, M., Park, B.H., Cense, B., Chen, T.C., Boer, J.F.d., 2007. Journal of Biomedical Optics 12 (4), 041205.
Nassif, N., Cense, B., Park, B.H., Yun, S.H., Chen, T.C., Bouma, B.E., Tearney, G.J., Boer, J.F.d., 2003. Optics Letters 29 (5), 480–482.
Özkumur, E., Needham, J.W., Bergstein, D.A., Gonzalez, R., Cabodi, M., Gershoni, J.M., Goldberg, B.B., Ünlü, M.S., 2008. Proceedings of National Academy of Sciences 105 (23), 7988–7992.
Piehler, J., Brecht, A., Gauglitz, G., 1996. Analytical Chemistry 68, 139–143.
Popescu, G., Deflores, L.P., Vaughan, J.C., Badizadegan, K., Iwai, H., Dasari, R.R., Feld, M.S., 2004. Optics Letters 29, 2503–2505.
Schena, M., 2005. Protein Microarrays. Jones & Bartlett Publishers.
Shumaker-Parry, J.S., Campbell, C.T., 2004. Analytical Chemistry 76 (4), 907–917.
Vollmer, F., Arnold, S., 2008. Nature Methods 5, 591–596.
Wegner, G.J., Wark, A.W., Lee, H.J., Codner, E., Saeki, T., Fang, S., Corn, R.M., 2004. Analytical Chemistry 76, 5667–5684.
Wilson, T., 1990. Confocal Microscopy. Academic Press, London.
Wu, S.Y., Ho, H.P., Law, W.C., Lin, C., Kong, S.K., 2004. Optics Letters 29, 2378–2380.
Yalcin, A., Popat, K.C., Aldridge, J.C., Desai, T.A., Hryniewicz, J., Chbouki, N., Little, B.E., King, O., Van, V., Chu, S.T., Gill, D., Anthes-Washburn, M.F., Ünlü, M.S., Goldberg, B.B., 2006. IEEE Journal of Selected Topics in Quantum Electronics 12, 148–155.
Ymeti, A., Greve, J., Lambeck, P.V., Wink, T., Hovell, S.W.F.M.V., Beumer, T.A.M., Wijn, R.R., Heideman, R.G., Subramaniam, V., Kanger, J.S., 2007. Nano Letters 7 (2), 394–397.
Zhao, M., Wang, X., Nolte, D.D., 2008. Optics Express 16 (10), 7102–7118.